Journal of Alloys and Compounds 687 (2016) 188–196

Contents lists available at ScienceDirect

Journal of Alloys and Compounds

journal homepage: http://www.elsevier.com/locate/jalcom

# *In situ* HEXRD study of a $Ca_{61}Al_{39}$ metallic glass

Štefan Michalik [a, *], Juraj Ďurišin [b], Dušan Balga [c, d], Karel Saksl [c, e], Martin Ďurišin [c], Michael Drakopoulos [a]

[a] Diamond Light Source Ltd., Harwell Science and Innovation Campus, Didcot, Oxfordshire OX11 0DE, UK
[b] Department of Technologies in Electronics, Faculty of Electrical Engineering and Informatics, Technical University of Košice, Park Komenského 2, 040 01 Košice, Slovak Republic
[c] Institute of Materials Research, Slovak Academy of Sciences, Watsonova 47, 040 01 Košice, Slovak Republic
[d] Faculty of Metallurgy, Technical University of Košice, Letna 9, 042 00 Košice, Slovak Republic
[e] Institute of Physics, Faculty of Science, P.J. Šafárik University, Park Angelinum 9, 041 54 Košice, Slovak Republic

ARTICLE INFO

*Article history:*
Received 9 February 2016
Received in revised form
1 June 2016
Accepted 9 June 2016
Available online 11 June 2016

*Keywords:*
Metallic glasses
Atomic scale structure
X-ray diffraction
Synchrotron radiation

ABSTRACT

High energy X-ray diffraction (HEXRD) was used to characterize the amorphous structure of the as-prepared binary $Ca_{61}Al_{39}$ (at.%) metallic glass and its evolution during thermal loading. The investigation was performed in both reciprocal and real space by means of the first diffuse peak (FDP) analysis and the reduced atomic pair distribution function (PDF) analysis, respectively. It was found that bond lengths of the atomic Ca–Ca and Ca–Al pairs of the as-prepared structure were 3.70 Å and 3.24 Å, respectively. The coordination number of the first coordination shell was estimated to be 11.9. The analysis of the FDP behaviour during thermal treatment proposed the existence of the relaxation temperature $T_r$ at 150 °C. Analysis of summations of all absolute differences between two consecutive intensity curves in the region of the FDP as a function of temperature revealed two crystallization temperatures at 280 °C and 305 °C. Products of a devitrification process were identified to be alike a triclinic $Ca_8Al_{13}$ and monoclinic $Ca_{13}Al_{14}$ phase.


## 1. Introduction

Ca-based metallic glasses (MGs) represent one group of disordered materials which have been attracting the attention of investigators during last three decades due to their unique mechanic properties [1], curious magnetic characteristics [2] and extraordinary thermodynamics features [3] compared with crystalline counterparts. Special interest in the Ca-based metallic glasses has been initialized by the very low density of this type of materials approaching 2.0 g/cm$^3$ [4]. Ca-based MGs have low Young's modulus (20–30 GPa) comparable to that of human bones proposing them as a suitable material for biomedical applications [5]. Within the classification of bulk metallic glasses (BMGs) introduced by Takeuchi and Inoue [6], Ca-based glasses constitute a new seventh group of BMGs consisting of alkaline metals (Ca and Mg) and late transition metals (such as Ag, Cu, Zn, and Ni). However it has recently been proved that Ca-based BMGs may also contain Al, Ga, Y and La-group metals [7]. Up to now several ternary (Ca–Mg–Zn, Ca–Mg–Cu, Ca–Mg–Al) and multicomponent systems of Ca-based MGs have successfully been prepared in a bulk form, some of them with diameters up to 4 mm [5,8,9]. The downside of Ca-based crystalline metallic alloys is their very low oxidation and corrosion resistance. Those characteristics are considerably improved when the alloy is prepared in a glassy state [8]. Additionally, it has been shown that the oxidation and corrosion resistance of Ca-based MGs is enhanced by the substitution of Zn with Cu and/or Al [10].

Generally, binary metallic alloys are considered to be unable to form bulk amorphous alloys due to not satisfying the confusion principle [11]. However, current experimental works have identified several binary systems, namely the Ca–Al [12], Cu–Zr [13], Cu–Hf [14], Ni–Nb [15] and Ni–Ta [16], able to produce BMGs in the form of rods and strips of minimal thickness of 1 mm despite the fact that binary systems do not follow Inoue's multielement rule requiring at least three different components [1]. Furthermore in many of those binary systems, the alloys with off-eutectic compositions have been found to have higher glass forming ability (GFA) than in-eutectic alloys [15,17,18]. This observation breaks another traditional empirical rule guidelining that alloys with

* Corresponding author.
*E-mail address:* stefan.michalik@diamond.ac.uk (Michalik).

http://dx.doi.org/10.1016/j.jallcom.2016.06.094

higher reduced glass transition temperature are better glass formers [19]. The better GFA of off-eutectic alloys has induced further concern in those extraordinary binary glassy systems.

In the eighties of the last century, investigations of various binary glassy Ca–Al alloys were forced by the aim to explain transport properties and calculate electronic structure of these amorphous systems [20–22]. The new interest in the binary Ca–Al amorphous system has been regained after the discovery that the glassy Ca–Al system can be prepared in a bulk form by Guo et al. [12]. In their work, they focused the attention on a Ca–Al glassy alloy of the eutectic composition ($Ca_{66.2}Al_{33.8}$, at.%). Their investigation was mainly carried out by means of differential scanning calorimetry. Very recently, the existence of a high pressure-induced amorphous-to-amorphous configuration change in $Ca_{(100-x)}Al_x$ for $x < 33.6$ at.%. metallic glasses has been reported by Lou et al. using *in situ* room-temperature high-pressure X-ray diffraction. This observation in addition supports interest in the binary glassy Ca–Al system.

The purpose of this work is to characterize the structure of the as-prepared $Ca_{61}Al_{39}$ metallic glass and its changes during heating below and above the crystallization temperature using high energy X-ray diffraction and X-ray reduced atomic pair distribution functions. On the one hand, X-ray diffraction has to reach at the expense of $Q$ resolution as high $Q$ values as possible to characterize an amorphous structure, on the other hand, revealing of devitrification products often requires much better $Q$ resolution than is normally obtained during diffraction experiments optimized for pair distribution function calculations. Therefore authors realized separately *in situ* HEXRD measurements in conditions designed for obtaining high $Q$ values and then in conditions of higher $Q$ resolution more suitable for observation of a crystalline structure.

## 2. Experimental procedure

### 2.1. Sample preparation

A master alloy was fabricated by vacuum arc-melting a mixture of high-purity Ca (99.5 at.%) and Al (99.7 at.%) metals. Chemical homogeneity of the master ingot was reached by multiple remelting. Ribbon specimens with the cross section of $0.03 \times 1$ mm$^2$ were prepared from the master ingot by a melt spinning technique. A jet of molten material formed by ejecting the melt under pressure of purified argon through an orifice impinged on the surface of a cooper wheel rotated with a surface velocity of 20 ms$^{-1}$. The final chemical composition of the as-prepared ribbons was controlled by the energy dispersive X-ray microanalysis.

### 2.2. DSC measurements

Thermal analysis measurements were performed using a Perkin-Elmer differential scanning calorimeter DSC 8500 at heating rate of 5 °C/min under a flow of purified argon.

### 2.3. HEXRD measurements

The high energy X-ray diffraction (HEXRD) experiments were carried out at the Joint Engineering, Environmental and Processing (I12-JEEP) beamline at Diamond Light Source Ltd., United Kingdom. The beamline can operate in polychromatic or monochromatic mode with a selectable energy between 53 keV and 150 keV. More details about the beamline can be found elsewhere [23]. Diffraction experiments were performed at three various energies, 90.54 keV ($\lambda = 0.1369$ Å), 83.59 keV ($\lambda = 0.1483$ Å) and 53.14 keV ($\lambda = 0.2333$ Å) using monochromatic mode. The X-ray radiation of higher energies (90.54 keV and 83.59 keV) was applied to cover $Q$-space up to high $Q$ values (above 20 Å$^{-1}$) enabling to characterize the investigated specimen using reduced atomic pair distribution functions. Using the beam energy of 53.14 keV improved the momentum resolution of the collected diffraction patterns. All diffraction experiments were done in transmission mode using a flat-panel Pixium RF4343 detector (2880 × 2881 pixels, pixel size of 148 × 148 μm). The beam size was $0.4 \times 0.4$ mm$^2$. The precise energy calibration was realized by measuring calibration data from a fine powder $CeO_2$ standard (NIST Standard Reference Material 674b) at different standard-to-detector distances. Following the approach of Hart et al. [24], X-ray energy and diffraction geometry were aligned from basic principles, requiring only a calibration sample and high-precision linear stage. Different sample-to-detector distances were set using a high precision stage, on which the detector was fixed. Once the beam energy was calibrated the detector was positioned at a desired distance. Then a standard NIST sample ($CeO_2$) was measured again to calibrate absolutely the sample-to-detector distance, the orthogonality of a detector with respect to an incoming beam and the position of a beam centre on the detector. With this it is possible to assign an accurate $Q$-values to each detector pixel. All those calibration procedures together with data integration along the radius of diffraction circles into $Q$-space were performed using the DAWN software [25].

In order to characterize the as-prepared state of the investigated glassy alloy a few pieces of ribbons were placed in a Kapton tube of 1 mm diameter. Then X-ray diffraction images were collected for one hour with acquisition time of 8 s for a pattern using the beam of 90.54 keV energy. Finally, all collected images (in total number of 450) were summed up to obtain high quality data with a low signal/noise ratio at high $Q$ values. The background signal (Kapton tube and air scattering) was measured at the same conditions as the sample in order to be subtracted from the sample signal.

The structural stability of the $Ca_{61}Al_{39}$ sample during thermal loading was investigated by the *in situ* HEXRD. The sample material placed inside of a quartz capillary with a diameter of 1 mm and a wall thickness of 0.01 mm was heated by a Linkam DSC600 furnace. *In situ* HEXRD measurements dedicated to atomic pair distribution function calculations were carried out using the beam energy of 83.59 keV. The sample-to-detector distance was 526 mm. The sample was heated from room temperature up to 590 °C at heating rate 5 °C/min. An empty quartz capillary was treated at the same way as the sample in order to collect the background signal at particular temperatures. Then the background signal was subtracted from the corresponding sample signal. In the case of the HEXRD measurement with higher $Q$ resolution, the sample-to-detector distance was 2557 mm and the beam energy was 53.14 keV. The specimen was heated from room temperature up to 225 °C at heating rate of 20 °C/min, then from 225 °C up to 550 °C at heating rate of 5 °C/min and finally cooled down to 50 °C at heating rate of 5 °C/min. During the sample heating/cooling, X-ray data were continuously collected. The recording time for obtaining a diffraction pattern was 24 s.

The phase analysis was realized using JCPDS PDF2 powder diffraction database with its interface implementation in the CMPR software [26] and using the ICSD database.

### 2.4. S(Q) and D(r) calculations

The total X-ray structure factor $S(Q)$ was directly extracted from the integrated data corrected for self-absorption, Compton scattering, fluorescence and multiply scattering applying the Faber-Ziman formalism [27]. Then the total X-ray reduced atomic pair distribution function $D(r)$ was calculated as a Fourier sine transformation of $Q[S(Q)-1]$

$$D(r) = \frac{2}{\pi}\int_{Q_{min}}^{Q_{max}} Q[S(Q)-1]\sin(rQ)\mathrm{d}Q \quad (1)$$

where $Q_{min}$ and $Q_{max}$ are boundaries of the scattering vector $Q$ ($Q = 4\pi\sin(\theta)/\lambda$; $\theta$ is half of the scattering angle) covered by XRD experiments, $r$ is the radial distance from the centre of an average atom in a sample. The number of atoms $N_C$ in an annulus of thickness $dr$ at a distance $r$ from another atom can be calculated as

$$N_C = \int_{r_1}^{r_2}\left(r^2 D(r) + 4\pi\rho_0 r^2\right)\mathrm{d}r \quad (2)$$

where $\rho_0$ is the average atomic number density. More information about $D(r)$ calculations and its related functions can be found elsewhere [28]. The conversion of the measured intensity curves $I(Q)$s into $S(Q)$s and then calculation of $D(r)$s were performed using the PDFGetX2 [29] and PDFGetX3 [30] program.

## 3. Experimental results and discussion

### 3.1. As prepared state of the $Ca_{61}Al_{39}$ alloy

The amorphicity of the as-prepared $Ca_{61}Al_{39}$ alloy was investigated by the HEXRD. The diffraction data obtained after the summation of 450 collected 2D images is presented in Fig. 1. The resultant diffraction pattern consists of a series of concentred diffuse rings with gradually reducing intensities. The image looks like a typical pattern expected to be observed for a fully glassy alloy. However a careful inspection of the diffraction image revealed an occurrence of several very weak scattered spots as can be seen in Fig. 1b) showing zoom of a selected part of the 2D image. Some of the most intensive scattered points are highlighted by red circles to emphasize their presence. After radial integration those scattered points are transformed into a 1D intensity curve as tiny Bragg peaks superpositioned on an amorphous sample signal. The intensity curve $I(Q)$ consists of a diffuse maximum centred at 2.19 $Å^{-1}$ followed by series of vanishing broad oscillations reflecting the amorphous character of the structure. Similarly to diffraction spots on the 2D diffraction image, the corresponding Bragg peaks are hardly detectable in the intensity curve. Inset in Fig. 1c displays the intensity $I(Q)$ in an interval of $Q$ values from 3 to 7 $Å^{-1}$. The emerging Bragg peaks are marked by diamond symbols. These very weak Bragg peaks were identified as those belonging to a single cubic CaO phase (#371497) using the JCPDS PDF2 database. It is well known that crystalline Ca is a highly reactive element. Despite the fact that Ca-based metallic glasses have improved corrosion resistance in contrast to Ca-based crystalline alloys [8], it could happen that the surface of the investigated alloy had gently corroded. A visual inspection of the ribbon surface revealed its shiny character proposing heavily any sample oxidation. Actually, the XRD technique was able to detect a small amount of CaO phase only due to using intensive synchrotron radiation which significantly improved a signal-noise ratio. The authors suppose that this very tiny fraction of the crystalline CaO phase did not influence their aim to investigate bulk structural changes of the binary $Ca_{61}Al_{39}$ metallic glass induced during thermal loading.

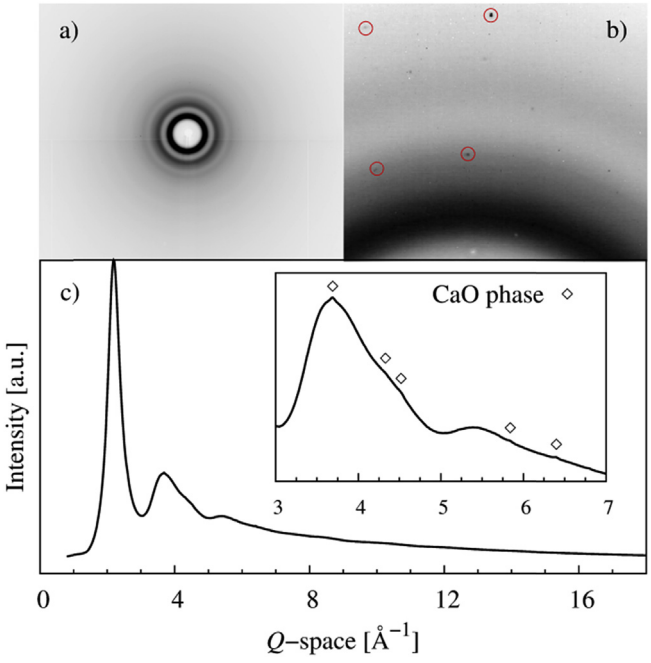


**Fig. 1. XRD patters of the as prepared alloy**: a) A whole 2D diffraction image collected by a flat plate detector, b) a small particular part of the 2D image displaying a few weak diffraction spots highlighted by red circles, c) an intensity curve obtained after full radial integration of the 2D image together with an insert showing a selected part of the intensity curve $I(Q)$. Diamonds symbols mark positions of revealed Bragg peaks belonging to a cubic CaO phase. (For interpretation of the references to colour in this figure legend, the reader is referred to the web version of this article.)

Applying all necessary intensity corrections and corresponding normalization following the Faber-Ziman formalism, the total X-ray structure factor $S(Q)$ was extracted up to 18 $Å^{-1}$. The $S(Q)$ function is presented in Fig. 2a. Although, the XRD data were collected up to 24 $Å^{-1}$ no oscillations could be observed above 17 $Å^{-1}$. The total X-ray reduced atomic pair distribution function $D(r)$ is shown in Fig. 2b). The usefulness of $D(r)$ comes from the fact that $D(r)$ represents a probability of finding an atom at a certain distance $r$ from an average atom. In other words, $D(r)$ directly contains information about interatomic spacing of individual atomic pairs of an investigated structure. Considering basic characteristics of $D(r)$ this function behaves like - $4\pi\rho_0 r$ as $r$ approaches 0 [28]. Fitting $D(r)$ part below 2.4 Å with a straight line (a green line in Fig. 2b) will determine the average atomic number density $\rho_0$. Data below 2.4 Å were fitted with the linear function using the nonlinear least-squares algorithm. From this fit, $\rho_0$ was estimated to be 0.030 ± 0.001 $Å^{-3}$. The uncertainty of $\rho_0$ was determined as the computational error of the fitted linear parameter. The analysis of the X-ray $D(r)$ function was mainly focused on a first broad maximum covering the region from 2.7 to 4.5 Å which represents a 1D projection of a first coordination shell.

As the investigated metallic alloy is of a binary type, three different atomic pairs, namely Ca–Ca, Ca–Al and Al–Al, are presented. The contribution of individual atomic pairs to the total D(r) function calculated from the HEXRD is not equal. It depends on the ability of a specific atomic pair to scatter X-rays. X-ray weights of atomic form factors calculated at Q = 0 are 0.56, 0.38 and 0.06 for Ca–Ca, Ca–Al and Al–Al pairs. The visibility of Al–Al atomic pairs is much smaller compared with contributions of Ca–Al and Ca–Ca pairs to the total X-ray D(r) function. It means that the total D(r) function obtained from HEXRD as an alone-standing/single source of the structural data would have difficulties to offer comprehensive information about Al–Al pairs because I(Q) is dominated by Ca–Ca and Ca–Al pairs. The detail of D(r) reflecting the first coordination shell is shown in Fig. 2c. It is immediately recognized that the maximum is split into two subpeaks suggesting the existence of two subshells. Therefore this maximum was fitted using two Gaussian functions. As can be seen in Fig. 2c), an excellent match between a fitting curve and experimental data was

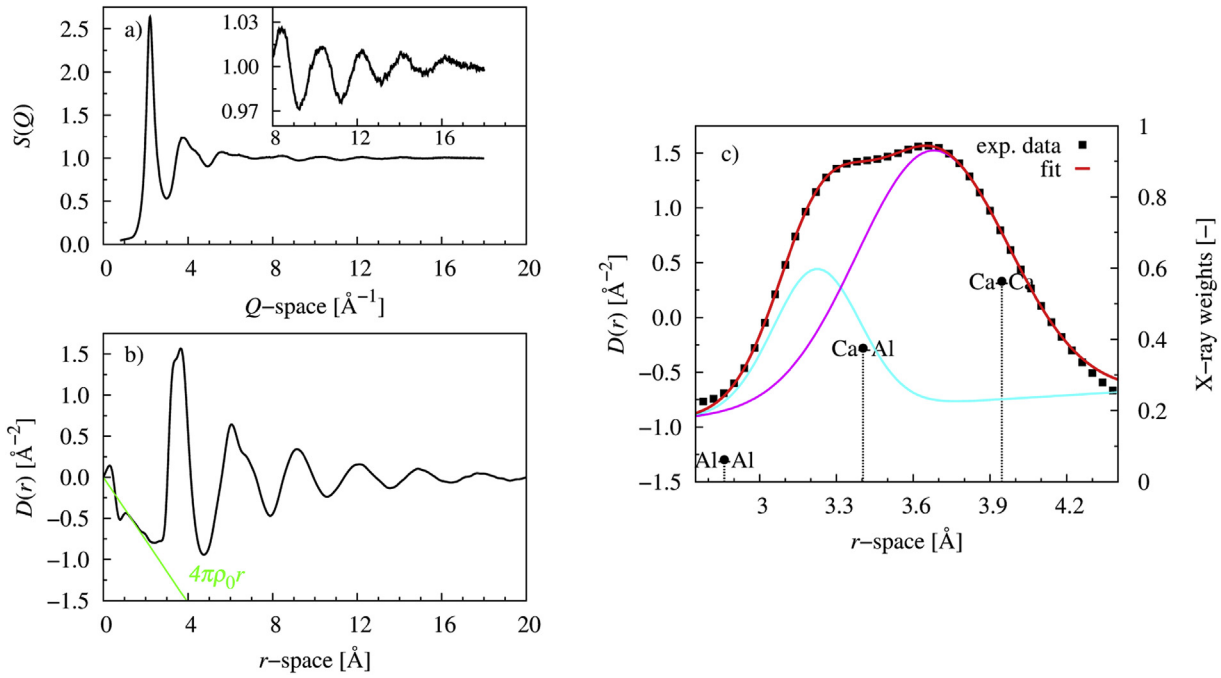


**Fig. 2. *S*(Q) and D(*r*) of the as prepared alloy**: a) The total structure factor *S*(Q) and b) reduced atomic pair distribution function *D*(*r*) of the as-prepared $Ca_{61}Al_{39}$ metallic glass. c) The selected region of *D*(*r*) corresponding to the first coordination shell (black squares) together with interatomic metallic (Goldschmidt) bond lengths and X-ray weights of Ca–Ca, Ca–Al and Al– Al atomic pairs. The red line represents the final fit of experimental data (black squares) using two independent Gaussian functions (cyan and magenta lines) at positions of 3.23 Å and 3.68 Å and linear background. (For interpretation of the references to colour in this figure legend, the reader is referred to the web version of this article.)

achieved. The Gaussian at 3.22 Å and Gaussian at 3.68 Å could be interpreted as representatives of subshells created by the closest Ca–Al and Ca–Ca atomic pairs, respectively. The positions of the Gaussians are compared with values of 3.404 Å for Ca–Al and 3.946 Å for Ca–Ca calculated as the sum of nominal metallic (Goldschmidt) atomic radii of an Al atom (1.431 Å) and Ca atom (1.973 Å), respectively. This observation shows that the bond lengths of Ca–Al and Ca–Ca atomic pairs are significantly shorter (5.1% and 6.7%, respectively) than values proposed by the simple model using the nominal sum of metallic atomic radii. It has been proposed by Quo [12] that a binary amorphous Ca–Al system could possess covalent features albeit this assumption was not supported by any direct experimental evidence. It was induced from the fact that chemical reactions between alkaline-earth metals (such as IIA group) and metals of IIIA group can exhibit clear features of covalent bonding for crystalline materials [31]. The analysis of the total X-ray *D*(*r*) function could offer a straight experimental indication of covalent character of bonds in the Ca–Al metallic glass. Furthermore, using eq. (2), the coordination number of the first coordination $N_C$ shell was estimated to be 11.9 ± 0.3[1].

Up to now 4 different crystalline phases of the Ca–Al binary system have been observed, namely cubic $CaAl_2$, tetragonal $CaAl_4$, triclinic $Ca_8Al_3$ and monoclinic $Ca_{13}Al_{14}$ [32]. It is interesting to compare *D*(*r*) of the as-prepared glassy sample with *D*(*r*)s of individual crystalline phases which were calculated using the PDFgui program [33] at the range of distances of the short and middle range ordering, see Fig. 3. It is immediately recognized that *D*(*r*)s of high symmetry phases totally differ from the one of the investigated sample. On the other hand, especially in the case of the triclinic $Ca_8Al_3$ phase, relatively good accordance is observed proposing structural similarities between the structure of the investigated glassy alloy and this triclinic phase.

### 3.2. Structural evolution of the $Ca_{61}Al_{39}$ alloy during thermal loading

The thermal stability of the glassy $Ca_{61}Al_{39}$ alloy was studied by the differential scanning calorimetry. The inspection of the DSC shown in Fig. 4a revealed the presence of a weak endothermic event at 255 °C corresponding to the glass temperature $T_G$. The endothermic event is followed by two strong exothermic peaks with onsets at $T_{X1}^{onstet} = 267$ °C and $T_{X2}^{onset} = 292$ °C corresponding to the onset of the first and second crystallization, respectively. Peak positions are at $T_{X1} = 274$ °C and $T_{X2} = 299$ °C. All these values are in accordance with ones reported by Gue [12]. It is remarkable to note that a curve resembling a DSC curve can be extracted from the XRD data by plotting the summation of all absolute differences between two consecutive intensity curves in the region of the FDP as a function of temperature. In other words, any differential curve $\Delta I_{T_n}(Q) = |I_{T_{n+1}}(Q) - I_{T_n}(Q)|$ is represented by a scalar value *A* obtained as an area under this $\Delta I_{T_n}$ curve. The obtained *A*(*T*) function is shown in Fig. 4b). Two crystallization maxima at 280 °C and 305 °C can immediately be recognized. They are almost perfectly consistent with maxima observed on the DSC curve. Additionally, it seems that it is possible to identify the $T_G$ temperature at 261 °C on the *A*(*T*) curve, see insets in Fig. 4a) and b). The relative shift of 6 °C between values obtained from the DSC curve and the *A*(*T*) function may be explained by using different furnaces during the DSC and XRD experiment. Furthermore the *A*(*T*) function exhibits the third maximum at 578 °C which might be attributed to the melting point of the studied sample. This maximum would have been appeared as an endothermic peak at the DSC curve if the DSC measurement had not been finished at 550 °C. On one hand, it is true that the DSC measurement directly contains information about the exothermic/endothermic character

[1] The $N_C$ uncertainty was estimated on the base of the $\rho_0$ uncertainty of ± 0.001.

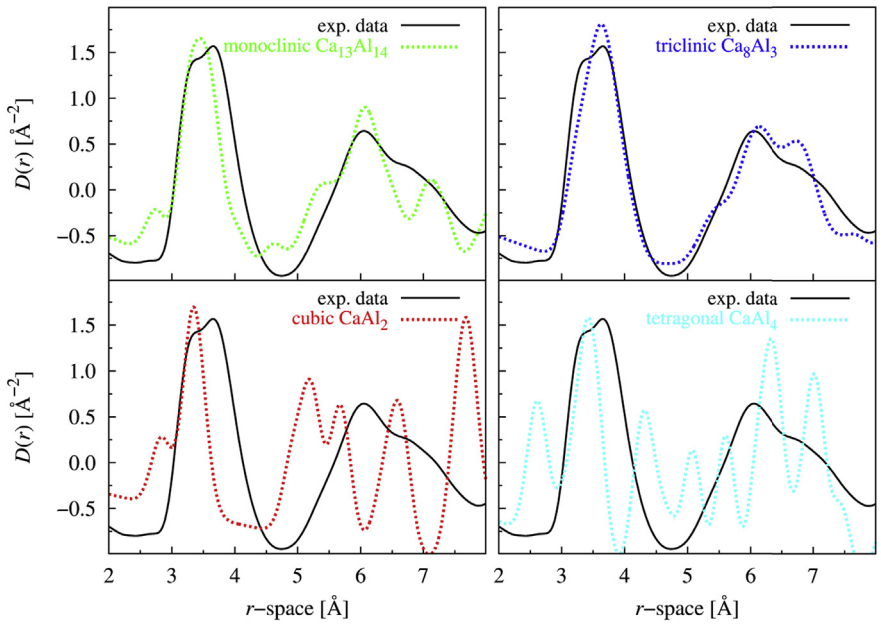


**Fig. 3. Comparison of *D*(*r*)s of glassy and crystalline alloys**: Comparison of $D(r)$ of the as-prepared glassy $Ca_{61}Al_{39}$ alloy and $D(r)$ of a monoclinic $Ca_{13}Al_{14}$ (top left), triclinic $Ca_8Al_3$ (top right), cubic $CaAl_2$ (bottom left) and tetragonal $CaAl_4$ (bottom right) crystalline phase.

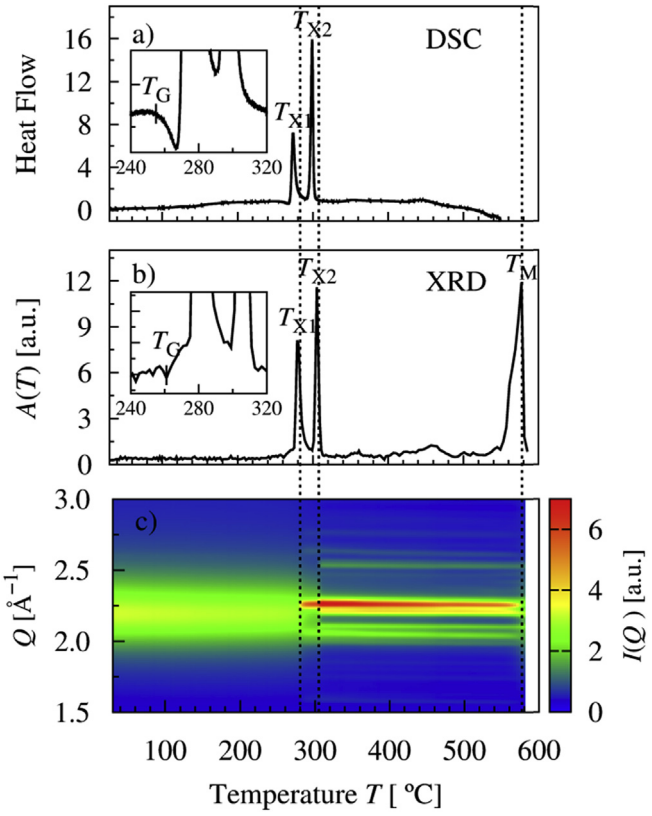


**Fig. 4. DSC, *A*(*T*) and *I*(*Q*) curves**: a) The DSC curve covering the temperature interval from room temperature up to 550 °C at heating rate of 5 °C/min, b) $A(T)$ curve and c) contour plot extracted from HEXRD patterns of the $Ca_{61}Al_{39}$ metallic glass obtained during thermal loading from room temperature up to 580 °C at heating rate of 5 °C/min.

of a reaction which is not the case of the $A(T)$ function. On the other hand, this information can be identified from the original intensity curves which are displayed in the form of a 2D map in Fig. 4c).

The behaviour of the amorphous state of the $Ca_{61}Al_{39}$ alloy below the crystallization was investigated by following the changes of the first diffuse peak (FDP) of intensity curves. The evolution of the relative position $Q$, broadening (full width at half maximum) $w$ and amplitude (intensity) $I$ of the FDP below the crystallization temperature is shown in Fig. 5. As it is expected due to heating the intensity of the FDP gradually decreases with increasing temperature. Broadening of the FDP is without any changes up to 150 °C. Then it starts significantly to narrow. At first glance this is a surprising behaviour. Usually diffraction peaks are expected to become broader as a function of rising temperature reflecting the increase of the thermal disordering. However, higher temperature may initialize a process of structural relaxation. The influence of annealing on structural relaxation processes of swift-ion irradiated Fe-based MGs were in detail studied by the authors using peak broadening in their recent work [34]. In the case of the investigated $Ca_{61}Al_{39}$ glass alloy, annealing reduces the stresses induced during the sample preparation by the melt-spinning technique. The observation of the peak narrowing reflects the structural recovery. It is interesting to mention that the DSC curve does not propose any changes around 150 °C. Another hint advocating the occurrence of structural variations at 150 °C is offered by following the FDP position. The FDP position is linearly shifted to lower $Q$ values as a function of temperature. This trend is altered in an opposite direction after reaching the temperature of 150 °C. Regarding an assumption that an average interatomic spacing $d$ could be proportional to $2\pi/Q_{max}$ [35], then the spacing is firstly slightly increased as a function of temperature and then is decreased. The $Q_0/Q_T$ ($d_T/d_0$) curve has a maximum at 150 °C which corresponds to the relaxation temperature $T_r$ of the investigated amorphous specimen (see Fig. 5). Likewise in this work, Bednarcik [36] demonstrated for La-based bulk metallic glasses that the relaxation temperature $T_r$ was detectable neither by the DSC nor by the dilatometry, it was only observable by using an *in situ* HEXRD technique. It has already been proved that the *in situ* HEXRD is sufficiently sensitive to detect the glass transition temperature following position changes of the FDP [37,38]. Despite the DSC calorimetry clearly indicates the $T_G$ at 255 °C, it is not possible to

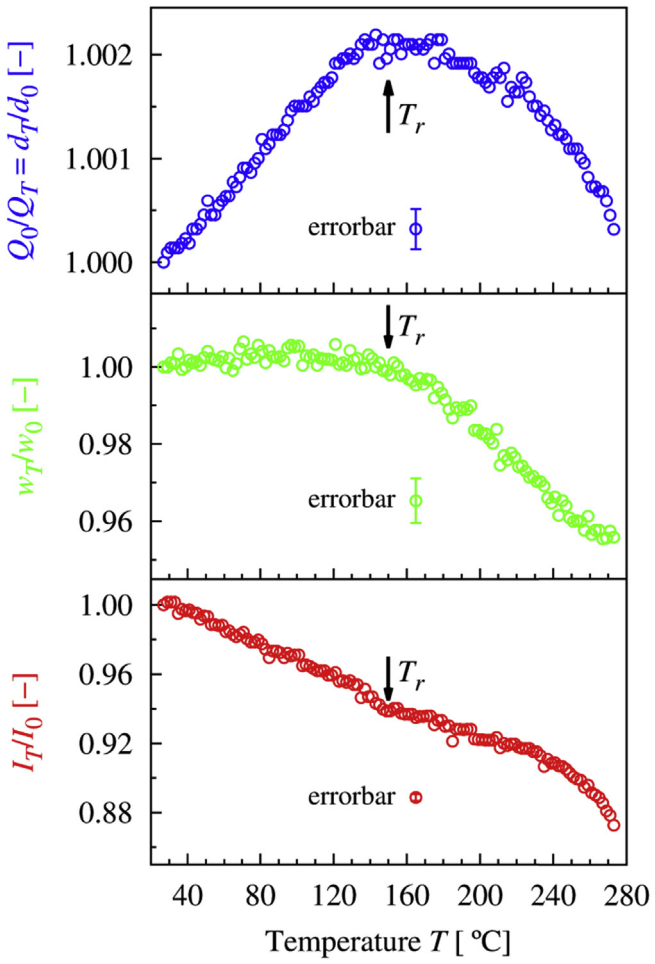


**Fig. 5. FDP temperature behaviour**: Relative changes of the profile parameters (peak position $Q$, peak width/broadening $w$ and peak amplitude/intensity $I$) of the FDP during thermal loading at heating rate of 5 °C/min.

assign $T_G$ using the $Q_0/Q_T$ curve extracted from diffraction presented in Fig. 5. It is probably caused by the fact that the relaxation maximum obscures the region of the $Q_0/Q_T$ curve where $T_G$ should be detectable. Moreover the separation between $T_G$ and $T_X$ is only 12 °C so it is difficult to identify the slope change of the $Q_0/Q_T$ curve with only a few data points.

The first type of the *in situ* heating HEXRD experiment was realized in configuration to cover high $Q$ values enabling to calculate reduced atomic pair distribution functions $D(r)$s. Because the collection time of one diffraction pattern was only 24 s, the data quality was limited at high $Q$ values. Therefore structure factors $S(Q)$s were only extracted up to 15 Å$^{-1}$. Still, the quality of the reduced atomic pair distribution function above 2.5 Å was comparable to the static HEXRD experiments. Fig. 6 displays $D(r)$ functions at different selected temperatures. It is observed that oscillations which were slowly dying at high $r$ values for an amorphous state start to be much more pronounced above the crystallization temperature. The appearance of new maxima reflects the formation of an ordered state in the investigated sample. $D(r)$ changes are much more pronounced for interatomic distances longer than 8 Å. On the other hand, the modification of the first maximum which corresponds to the first coordination shell is not so prominent. Therefore the fitting model of the first coordination shell proposed for the as-prepared state was used to investigate variations of the first coordination shell during the devitrification

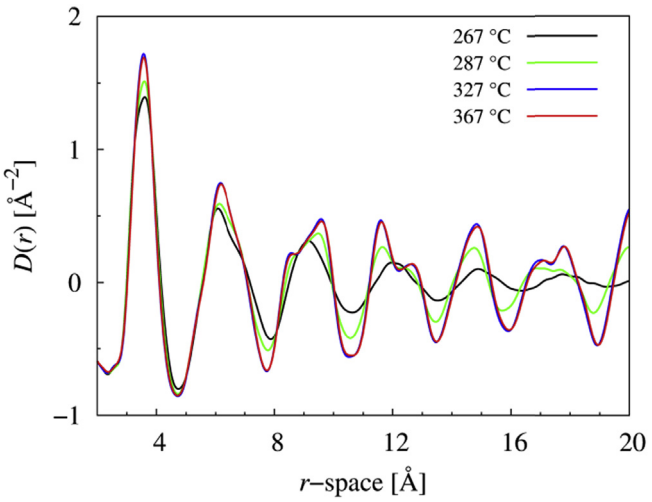


**Fig. 6. $D(r)$ at various temperatures**: The reduced atomic pair distribution function $D(r)$ for selected temperatures demostrating the crystallization process of the $Ca_{61}Al_{39}$ alloy. (For interpretation of the references to colour in this figure legend, the reader is referred to the web version of this article.)

process as well. Fig. 7 displays the temperature evolution of parameters (relative position $r_T/r_0$, broadening $w_T/w_0$ and intensity $I_T/I_0$) of two Gaussian functions used to describe Ca–Ca and Ca–Al atomic in the first coordination shell. Unlike in reciprocal space, the

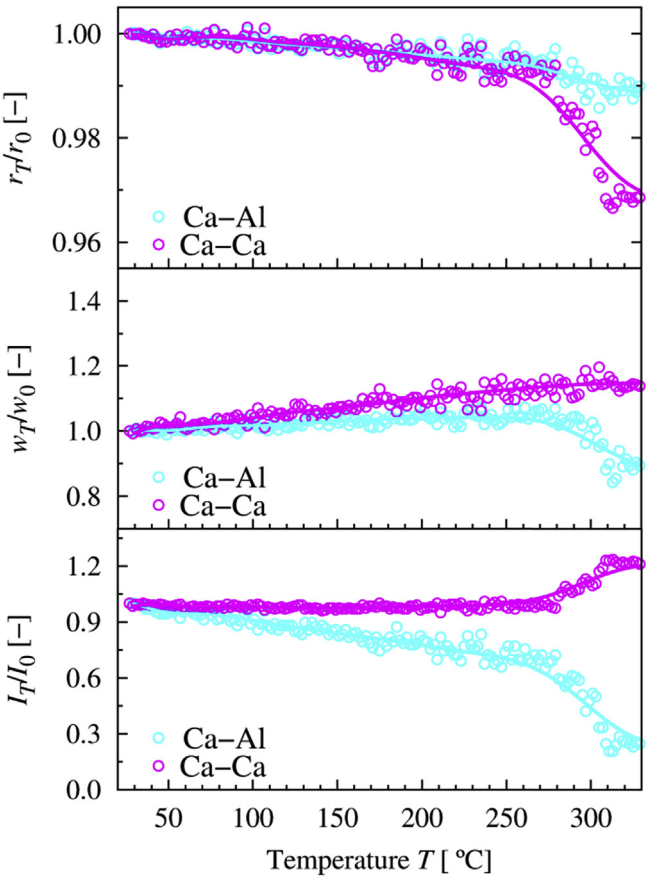


**Fig. 7. $D(r)$ first maximum behaviour**: The temperature evolution of profile parameters of two Gaussians used to model the first maximum of $D(r)$ below and around crystallization temperatures. (For interpretation of the references to colour in this figure legend, the reader is referred to the web version of this article.)

behaviour of all those parameters is smooth without any indication of variations around 150 °C. It is seen that interatomic Ca–Ca and Ca–Al bond lengths firstly slightly decrease when temperature increases. Unlike the $Q_0/Q_T = d_T/d_0$ dependence, no maximum is detectable around 150 °C on the $r_T/r_0$ curve. This discrepancy between the results obtained from reciprocal and real space is not yet fully understood. It has recently been proposed that position changes of the FDP in $Q$-space reflect mostly medium and longer range of interatomic correlations while the first maximum of the $D(r)$ function reveals gentle structural modifications occurring in the nearest atomic neighbourhood [39,40]. The sudden drop of the $r_T/r_0$ dependence, especially for Ca–Ca bonds, is observed at 280 °C which correlates with the temperature of the first crystallization. The average Ca–Ca and Ca–Al bond lengths were changed from 3.70 Å to 3.64 Å and from 3.24 Å to 3.18 Å, respectively, comparing the room temperature and temperature of 330 °C. The determination of coordination number changes of the first coordination shell during thermal loading is not straightforward as one might expect. As can be seen from eq. (2), knowledge of the average atomic number density $\rho_0$ is required to calculate it. The value of $\rho_0$ has already been determined from $D(r \rightarrow 0)$ of the as-prepared specimen at room temperature $T_0$. It is reasonable to expect that the sample density may differ as temperature increases. As consequence, the temperature behaviour of $\rho_0$ should be known to obtain correct values of $N_C$. Due to limitations of data collection (short exposure time) during the *in situ* HEXRD, it was not possible to extract $\rho_0(T)$ values using the part of $D(r)$ below 2.5 Å$^{-1}$ at particular temperatures. Zeng very recently proved that $\rho_0$ of a metal glass varies with 5/2 power of the FDP position when external pressure was applied using *in situ* high pressure HEXRD measurements [41]. Following this approach the atomic number density $\rho_0(T)$ was scaled as a function of temperature using a noncubic power law $\rho_0(T) = \rho_0(T_0)[Q(T_0)/Q(T)]^{5/2}$, where $\rho_0(T_0) = 0.03$ Å$^{-3}$ and Q($T$) and Q($T_0$) are positions of the FDP at optional temperature $T$ and room temperature $T_0$, respectively. For comparison purposes, $N_C(T)$ was calculated when $\rho_0$ had been considered to be constant during the whole temperature interval (red colour) and when $\rho_0$ had been modified using the noncubic power law (green colour), see Fig. 8. Once $\rho_0$ was considered to be temperature dependent it is possible to recognize a change in the behaviour of $N_C$ around 150 °C. Firstly, $N_C$ continuously decreases from 11.92 to 11.82 reflecting increase of thermal disordering. Then $N_C$ is stabilized in temperature interval from 150 to 260 °C. This stabilization could be caused by the sample structural recovery which competes with the increase of thermal disordering.

Finally, the *in situ* HEXRD experiment was carried out in the mode enabling $Q$ resolution as high as possible at conditions of the I12-JEEP beamline (the lowest reachable energy and the largest reachable sample-to-detector distance). Fig. 9 shows a contour plot extracted from HEXRD patterns collected during sample heating from room temperature up to 550 °C and cooling back down to room temperature. As it can be seen, the diffraction patterns consist of many overlapping Bragg peaks after crystallization proposing the formation of at least one low symmetry structure during the devitrification process. The phase analysis certainly excluded the presence of highly symmetric cubic and tetragonal Ca–Al phases as dominant devitrification products. Additionally, the authors have investigated all accessible aluminium and calcium oxides within JCPDS PDF2 database. None of them was able to index the major peaks in an $Q$ interval from 1.75 Å to 3.75 Å. The phase analysis proposes the formation of phases similar to a triclinic $Ca_8Al_3$ phase and monoclinic $Ca_{13}Al_{14}$ phase during the first and second crystallization (280 °C and 305 °C). Additionally, it is possible to observe significant peak intensity variations and improved peak separation around temperature 475 °C. Actually both the DSC curve and $A(T)$ function have a small peak at this temperature confirming some structural changes. During sample cooling the diffraction patterns do not exhibit other qualitative changes. Fig. 9 displays the intensity curve $I(Q)$ obtained from the sample at room temperature after

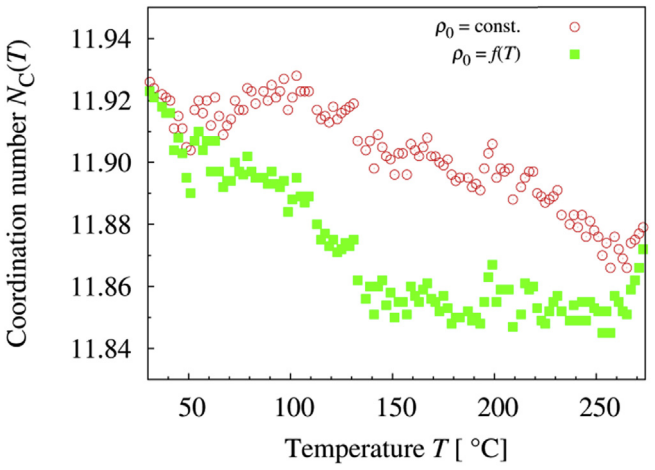


**Fig. 8. Coordination number evolution**: The coordination number of the first coordination shell $N_C$ as a function of temperature considering the average atomic number density to be constant (red circle points), $\rho_0$ = const., and to be temperature dependent (green square points), $\rho_0 = f(T)$. (For interpretation of the references to colour in this figure legend, the reader is referred to the web version of this article.)

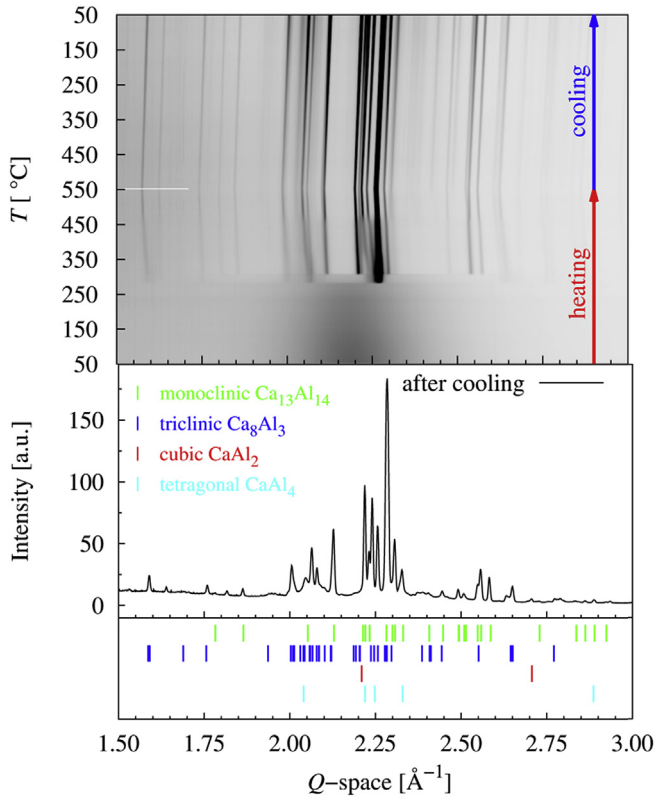


**Fig. 9. Devitrification process**: The contour plot of 3D HEXRD patterns collected during a heating and cooling cycle (top) and the 1D intensity curve of the sample obtained at room temperature after performing the complete heating and cooling treatment (bottom). Bragg peak positions of different binary Ca–Al phases are shown below the intensity curve. (For interpretation of the references to colour in this figure legend, the reader is referred to the web version of this article.)

performing the whole thermal cycle and positions of Bragg peaks of different Ca–Al phases for comparison. It is necessary to mention that the match between the suggested triclinic and monoclinic phase and collected diffraction profiles is still far away to be perfect especially for peak intensities. It can be concluded that the structure of devitrification products is beyond to be a simple one.

## 4. Conclusion

The structure of the $Ca_{61}Al_{39}$ metallic glass was investigated by high energy X-ray diffraction using synchrotron radiation. The analysis of the total X-ray reduced atomic pair distribution function $D(r)$ of the as-prepared specimen revealed meaningfully shorter bonds of Ca–Ca and Ca–Al atomic pairs (6.7% and 5.1%, respectively) as predicted on the base of nominal metallic atomic radii of Ca and Al atoms. This observation proposes covalent character of Ca–Ca and Ca–Al bonds. The slight decreasing of Ca–Ca and Ca–Al bond lengths was observed as a function of temperature below the crystallization. During the crystallization, the changes of the first maximum of $D(r)$ functions suggested additional shortening of Ca–Ca bond lengths. The coordination number of the first coordination shell of the investigated sample was estimated to be 11.9. Firstly the coordination number slightly decreases as temperature rises up to 150 °C and then remains constant. The analysis of the FDP in the reciprocal space indicated the occurrence of structural variations of the amorphous state at 150 °C. Those changes of the FDP were attributed to relaxation processes suggesting structural recovery of the glassy alloy. The HEXRD and DSC data confirmed two crystallization temperatures (at 280 °C and 305 °C) during devitrification. It was demonstrated that the summation of all absolute differences between two consecutive intensity curves in the region of the FDP as a function of temperature can be used to obtain a similar curve to a DSC one. The phase analysis proposed formation of phases similar to a triclinic $Ca_8Al_3$ and monoclinic $Ca_{13}Al_{14}$ phase.

The obtained XRD data were insufficiently sensitive to Al–Al atomic pairs due to low X-ray scattering ability of Al compared with Ca. Therefore we are still far away from obtaining a complete picture of the local atomic arrangement in the $Ca_{61}Al_{39}$ amorphous alloy. X-ray absorption spectroscopy and neutron diffraction should be added to the toolkit of applied techniques. However their realization is not straightforward for this type of the sample material.

The temperature evolution of profile parameters of two Gaussians used to model the first maximum of $D(r)$ below and around crystallization temperatures.

## Acknowledgements

K. Saksl, D. Balga and M. Ďurišin are grateful to the Scientific Grant Agency of the Ministry of Education, Science, Research and Sport of the Slovak Republic and the Slovak Academy of Sciences (VEGA Project No. 2/0021/16) and to the APVV-14-0085 project for the financial support of this work. J. Ďurišin is grateful to the Scientific Grant Agency of the Ministry of Education, Science, Research and Sport of the Slovak Republic and the Slovak Academy of Sciences (VEGA Project No. 1/0776/14) and to the APVV-14-0085 project for the financial support of this work.

## References

[1] A. Inoue, Stabilization of metallic supercooled liquid and bulk amorphous alloys, Acta Mater. 48 (2000) 279–306, http://dx.doi.org/10.1016/S1359-6454(99)00300-6.
[2] M.E. McHenry, M.A. Willard, D.E. Laughlin, Amorphous and nanocrystalline materials for applications as soft magnets, Prog. Mater. Sci. 44 (1999) 291–433.
[3] E. Bakke, R. Busch, W.L. Johnson, No Title, Appl. Phys. Lett. 67 (1995) 3260.
[4] V. Keppens, Z. Zhang, O.N. Senkov, D.B. Miracle, Localized Einstein modes in Ca-based bulk metallic glasses, Philos. Mag. 87 (2007) 503–508, http://dx.doi.org/10.1080/14786430600857353.
[5] B.R. Nowosielski, A. Borowski, A. Guwer, Fabrication of ternary Ca-Mg-Zn bulk metallic glasses, J. Achiev. Mater. Manuf. Eng. 56 (2013) 67–74.
[6] A. Takeuchi, A. Inoue, Classification of bulk metallic glasses by atomic size difference, heat of mixing and period of constituent elements and its application to characterization of the main alloying element, Mater. Trans. 46 (2005) 2817–2829, http://dx.doi.org/10.2320/matertrans.46.2817.
[7] O.N. Senkov, D.B. Miracle, V. Keppens, P.K. Liaw, Development and characterization of low-density Ca-Based bulk metallic glasses: an overview, Metall. Mater. Trans. A 39 (2008) 1888–1900, http://dx.doi.org/10.1007/s11661-007-9334-z.
[8] B.R. Barnard, P.K. Liaw, R.A. Buchanan, O.N. Senkov, D.B. Miracle, Oxidation behavior of Ca-Based bulk amorphous materials, Mater. Trans. 48 (2007) 1870–1878, http://dx.doi.org/10.2320/matertrans.MJ200744.
[9] O.N. Senkov, J.M. Scott, D.B. Miracle, Development of low density Ca-Mg-Al-Based bulk metallic glasses, Mater. Trans. 48 (2007) 1610–1616, http://dx.doi.org/10.2320/matertrans.MJ200731.
[10] J. Dahlman, O.N. Senkov, J.M. Scott, D.B. Miracle, Corrosion properties of Ca based bulk metallic glasses, Mater. Trans. 48 (2007) 1850–1854, http://dx.doi.org/10.2320/matertrans.MJ200732.
[11] P.J. Desré, On the effect of the number of components on glass-forming ability of alloys from the liquid state: application to the new generation of multicomponent bulk glasses, Mater. Trans. JIM 38 (1997) 583–588. https://www.jim.or.jp/journal/e/38/07/583.html.
[12] F.Q. Guo, S.J. Poon, G.J. Shiflet, CaAl-based bulk metallic glasses with high thermal stability, Appl. Phys. Lett. 84 (2004) 37, http://dx.doi.org/10.1063/1.1637940.
[13] D. Wang, Y. Li, B.B. Sun, M.L. Sui, K. Lu, E. Ma, Bulk metallic glass formation in the binary Cu–Zr system, Appl. Phys. Lett. 84 (2004) 4029, http://dx.doi.org/10.1063/1.1751219.
[14] L. Xia, D. Ding, S.T. Shan, Y.D. Dong, The glass forming ability of Cu-rich Cu–Hf binary alloys, J. Phys. Condens. Matter 18 (2006) 3543–3548, http://dx.doi.org/10.1088/0953-8984/18/15/002.
[15] L. Xia, W.H. Li, S.S. Fang, B.C. Wei, Y.D. Dong, Binary Ni–Nb bulk metallic glasses, J. Appl. Phys. 99 (2006) 026103, http://dx.doi.org/10.1063/1.2158130.
[16] Y. Wang, Q. Wang, J. Zhao, C. Dong, Ni–Ta binary bulk metallic glasses, Scr. Mater. 63 (2010) 178–180, http://dx.doi.org/10.1016/j.scriptamat.2010.03.044.
[17] I.A. Figueroa, J.D. Plummer, G.A. Lara-Rodriguez, O. Novelo-Peralta, I. Todd, Metallic glass formation in the binary Cu–Hf system, J. Mater. Sci. 48 (2013) 1819–1825, http://dx.doi.org/10.1007/s10853-012-6946-5.
[18] D. Wang, Y. Li, B.B. Sun, M.L. Sui, K. Lu, E. Ma, Bulk metallic glass formation in the binary Cu–Zr system, Appl. Phys. Lett. 84 (2004) 4029, http://dx.doi.org/10.1063/1.1751219.
[19] D. Turnbull, Under what conditions can a glass be formed? Contemp. Phys. 10 (1969) 473–488.
[20] S.R. Nagel, U.M. Gubler, C.F. Hague, J. Krieg, R. Lapka, P. Oelhafen, et al., Electronic structure studies of CaxAl1−x metallic glasses, Phys. Rev. Lett. 49 (1982) 575–578, http://dx.doi.org/10.1103/PhysRevLett.49.575.
[21] C.L. Tsai, F.C. Lu, Electronic transport properties of La–Al and Ca–Al metallic glasses, J. Non. Cryst. Solids 61-62 (1984) 1403–1408, http://dx.doi.org/10.1016/0022-3093(84)90740-3.
[22] J. Laakkonen, R.M. Nieminen, Resistivity of Ca-Al metallic glasses, Phys. Rev. B 34 (1986) 567–577, http://dx.doi.org/10.1103/PhysRevB.34.567.
[23] M. Drakopoulos, T. Connolley, C. Reinhard, R. Atwood, O. Magdysyuk, N. Vo, et al., I12: the Joint engineering, environment and processing (JEEP) beamline at diamond Light source, J. Synchrotron Radiat. 22 (2015) 828–838, http://dx.doi.org/10.1107/S1600577515003513.
[24] M.L. Hart, M. Drakopoulos, C. Reinhard, T. Connolley, Complete elliptical ring geometry provides energy and instrument calibration for synchrotron-based two-dimensional X-ray diffraction, J. Appl. Crystallogr. 46 (2013) 1249–1260, http://dx.doi.org/10.1107/S0021889813022437.
[25] M. Basham, J. Filik, M.T. Wharmby, P.C.Y. Chang, B. El Kassaby, M. Gerring, et al., Data analysis WorkbeNch ( DAWN ), J. Synchrotron Radiat. 22 (2015) 853–858, http://dx.doi.org/10.1107/S1600577515002283.
[26] B.H. Toby, CMPR – a powder diffraction toolkit, J. Appl. Crystallogr. 38 (2005) 1040–1041, http://dx.doi.org/10.1107/S0021889805030232.
[27] T.E. Faber, J.M. Ziman, A theory of the electrical properties of liquid metals, Philos. Mag. 11 (1965) 153–173.
[28] T. Egami, S.J.L. Billinge, Underneath the Bragg Peaks: Structural Analysis of Complex Materials, Pergamon, 2003.
[29] X. Qiu, J.W. Thompson, S.J.L. Billinge, {PDFgetX2}_ A {GUI} driven program to obtain the pair distribution function from X-ray powder diffraction data, J. Appl. Cryst. 37 (2004) 678.
[30] P. Juhás, T. Davis, C.L. Farrow, S.J.L. Billinge, PDFgetX3 : a rapid and highly automatable program for processing powder diffraction data into total scattering pair distribution functions, J. Appl. Crystallogr. 46 (2013) 560–566, http://dx.doi.org/10.1107/S0021889813005190.
[31] G.J. Miller, Chemistry, Structure and Bonding of Zintl Phases and Ions, VCH, New York, USA, 1996.
[32] B. Huang, J.D. Corbett, Two new binary Calcium–Aluminum compounds: Ca 13 Al 14, with a novel two-dimensional aluminum network, and Ca 8 Al 3, an Fe 3 Al-Type analogue 1, Inorg. Chem. 37 (1998) 5827–5833, http://dx.doi.org/10.1021/ic980656h.

[33] C.L. Farrow, P. Juhas, J.W. Liu, D. Bryndin, E.S. Božin, J. Bloch, et al., PDFfit2 and PDFgui: computer programs for studying nanostructure in crystals, J. Phys. Condens. Matter 19 (2007) 335219, http://dx.doi.org/10.1088/0953-8984/19/33/335219.

[34] S. Michalik, J. Michalikova, M. Pavlovic, P. Sovak, H.-P. Liermann, M. Miglierini, Structural modifications of swift-ion-bombarded metallic glasses studied by high-energy X-ray synchrotron radiation, Acta Mater. 80 (2014) 309–316, http://dx.doi.org/10.1016/j.actamat.2014.07.072.

[35] T. Hufnagel, R. Ott, J. Almer, Structural aspects of elastic deformation of a metallic glass, Phys. Rev. B 73 (2006) 064204, http://dx.doi.org/10.1103/PhysRevB.73.064204.

[36] J. Bednarcik, S. Michalik, M. Sikorski, C. Curfs, X.D. Wang, J.Z. Jiang, et al., Thermal expansion of a La-based bulk metallic glass: insight from in situ high-energy x-ray diffraction, J. Phys. Condens. Matter 23 (2011) 254204.

[37] J. Bednarcik, C. Curfs, M. Sikorski, H. Franz, J.Z. Jiang, Thermal expansion of La-based BMG studied by in situ high-energy X-ray diffraction, J. Alloys Compd. 504 (2010) S155–S158.

[38] A.R. Yavari, A. Le Moulec, A. Inoue, N. Nishiyama, N. Lupu, E. Matsubara, et al., Excess free volume in metallic glasses measured by X-ray diffraction, Acta Mater. 53 (2005) 1611–1619.

[39] J. Bednarcik, S. Michalik, V. Kolesar, U. Rütt, H. Franz, In situ XRD studies of nanocrystallization of Fe-based metallic glass: a comparative study by reciprocal and direct space methods, Phys. Chem. Chem. Phys. 15 (2013) 8470–8479, http://dx.doi.org/10.1039/c3cp44445g.

[40] J. Bednarcik, S. Michalik, M. Sikorski, C. Curfs, X.D. Wang, J.Z. Jiang, et al., Thermal expansion of a La-based bulk metallic glass: insight from in situ high-energy x-ray diffraction, J. Phys. Condens. Matter 23 (2011) 254204, http://dx.doi.org/10.1088/0953-8984/23/25/254204.

[41] Q. Zeng, Y. Kono, Y. Lin, Z. Zeng, J. Wang, S.V. Sinogeikin, et al., Universal fractional noncubic power law for density of metallic glasses, Phys. Rev. Lett. 112 (2014) 185502, http://dx.doi.org/10.1103/PhysRevLett.112.185502.